



ISTITUTO NAZIONALE DI RICERCA METROLOGICA Repository Istituzionale

Phase transformations and magnetostriction in Fe_{100-x}Gax bulk alloys

Original

Phase transformations and magnetostriction in Fe_{100-x}Gax bulk alloys / Coisson, M; N'Dri, Kd; Diallo, L; Olivetti, Es; Martino, L; Sasso, Cp; Celegato, F; Barrera, G; Pasquale, M; Rizzi, P; Malandrino, M; Nakonechna, O; Cuvilly, F; Tiberto, P; Juraszek, J; Bahamida, S; Fnidiki, A. - In: JOURNAL OF APPLIED PHYSICS. - ISSN 0021-8979. - 132:18(2022), p. 183912. [10.1063/5.0097930]

Availability:

This version is available at: 11696/76241 since: 2023-03-01T15:23:46Z

Publisher:

AIP Publishing

Published

DOI:10.1063/5.0097930

Terms of use:

This article is made available under terms and conditions as specified in the corresponding bibliographic description in the repository

Publisher copyright















AIP

This article may be downloaded for personal use only. Any other use requires prior permission of the author and AIP Publishing. This article may be found at DOI indicated above.

(Article begins on next page)

RESEARCH ARTICLE | NOVEMBER 14 2022

Phase transformations and magnetostriction in $\text{Fe}_{100-x}\text{Ga}_x$ bulk alloys

Marco Coïsson  ; Kouassi Dakmak N'Dri; Lindor Diallo ; Elena S. Olivetti ; Luca Martino; Carlo P. Sasso ; Federica Celegato ; Gabriele Barrera ; Massimo Pasquale ; Paola Rizzi ; Mery Malandrino ; Olha Nakonechna ; Fabien Cuvilly; Paola Tiberto ; Jean Juraszek ; Saïda Bahamida; Abdeslem Fnidiki 



Journal of Applied Physics 132, 183912 (2022)
<https://doi.org/10.1063/5.0097930>



CrossMark

AIP Advances

Why Publish With Us?

	25 DAYS average time to 1st decision		740+ DOWNLOADS average per article		INCLUSIVE scope
---	--	---	--	---	---------------------------

[Learn More](#) 

















Phase transformations and magnetostriction in $\text{Fe}_{100-x}\text{Ga}_x$ bulk alloys

Cite as: J. Appl. Phys. **132**, 183912 (2022); doi: 10.1063/5.0097930

Submitted: 3 May 2022 · Accepted: 12 October 2022 ·

Published Online: 14 November 2022



Marco Coisson,^{1,a)}  Kouassi Dakmak N'Dri,²  Lindor Diallo,³  Elena S. Olivetti,¹  Luca Martino,¹  Carlo P. Sasso,¹ 
Federica Celegato,¹  Gabriele Barrera,¹  Massimo Pasquale,¹  Paola Rizzi,³  Mery Malandrino,³ 
Olha Nakonechna,⁴  Fabien Cuvilly,⁴  Paola Tiberto,¹  Jean Juraszek,⁴  Saïda Bahamida,⁵ and Abdeslem Fridiki⁴ 

AFFILIATIONS

¹INRIM, Advanced Materials and Life Sciences Division, Torino, Italy

²Faculty of Science and Technology, University of Lorraine, Nancy, France

³Chemistry Department, University of Torino, Torino, Italy

⁴UNIROUEN, INSA Rouen, CNRS, GPM, Normandie Université, 76000 Rouen, France

⁵Research Unit UR-MPE, University of Boumerdes, 35000 Boumerdes, Algeria

^{a)}Author to whom correspondence should be addressed: m.coisson@inrim.it

ABSTRACT

Fe–Ga alloys, containing 18, 21, and 23 at.% of Ga, were prepared in bulk form. In their as-cast state, they display a small magnetostriction, that is strongly improved after annealing at 1000 °C for 24 h, and subsequent rapid cooling. Multiple characterization techniques, such as x-ray diffraction, differential scanning calorimetry, Mössbauer spectroscopy, temperature-dependent magnetization curves, hysteresis loops, magnetic force microscopy, and magnetostriction measurements, were exploited in synergy to gain a deep understanding of the structure–property relationships in the studied alloys, before and after annealing. The A2 phase, which is favored in the lower range of compositions and is promoted at the expense of the D0₃ one by annealing, is responsible for characteristic dendritic and maze magnetic domains, and for the strong improvement of the magnetostriction, which almost reaches 240 ppm (transverse configuration) in the alloys with 18 at.% of Ga, after annealing.

Published under an exclusive license by AIP Publishing. <https://doi.org/10.1063/5.0097930>

I. INTRODUCTION

Large magnetostriction and magnetoelastic coupling are properties extensively sought after because of their exploitability in low power consumption devices,^{1,2} energy conversion,³ and spintronics.^{4,5} Many alloys displaying large magnetostriction coefficients contain rare earths,⁶ whereas Fe–Ga systems, being rare earths free, have attracted attention because of their significant magnetostrictive response, coupled with good corrosion resistance and mechanical hardness.⁷

Magnetostriction is particularly significant in Fe-rich alloys, with Ga content approximately equal to 19% and 27%.^{7,8} In this range of compositions, the Fe–Ga binary system is characterized by the possible presence of multiple phases,^{9–12} whose complex interplay strongly affects the magnetostrictive response. The stabilization of the A2 or D0₃ phases by means of additional species in the alloy, like Tb^{13–15} or Ce,¹⁶ turned out to be particularly effective to

enhance magnetostriction, but partially defeats the purpose of getting rid of rare earths. However, a careful tailoring of the alloy microstructure can also lead to remarkable magnetostrictive properties,¹⁷ as well as the development, in thin films, of an ordered crystal growth on Si, MgO, or GaAs substrates,^{18,19} of six layer modulated monoclinic phases at the boundaries of the dominant bcc phase,²⁰ of Ga–Ga pairs in the A2 phase,²¹ or even of a polycrystalline, non oriented, dominant D0₃ phase, in spite of its tendency to minimize the Ga–Ga pairs.^{18,21–23}

Despite the Fe–Ga binary system is studied for many decades, its equilibrium phase diagram is still under assessment. Recently, Mohamed *et al.*²⁴ proposed a revisited version of the Fe-rich side of the phase diagram by comparing four different previous versions with their experimental data about a considerable amount of compositions, suggesting that some phase boundaries should be shifted. Besides, one should consider that in as-cast samples equilibrium conditions are rarely attained and the presence of quenched

05 JULY 2023 13:44:34

metastable phases should always be considered. Thus, a metastable phase diagram such as the one in Ref. 9 is often more appropriate in determining the sample phase composition and transformations. In addition, as will be discussed later, distinguishing between the disordered A2 and the ordered D0₃ phase is extremely difficult and requires sophisticated characterization techniques, such as Selected Area Electron Diffraction (SAED)²⁵ or high energy x-ray diffraction.²⁶ For these reasons, since the magnetostrictive properties are strictly dependent on the phase composition and stability, studies aiming at contributing to a comprehensive assessment of the structure–property relationships in the Fe–Ga alloy system are particularly valuable.

Within this context, the present work performs a detailed study on the microstructure and on the magnetic and magnetostrictive properties of Fe_{100-x}Ga_x (with $x = 18, 21, \text{ and } 23$) bulk alloys, through a combination of multiple techniques, including x-ray diffraction, conversion electron Mössbauer spectroscopy, differential scanning calorimetry, thermomagnetic curves, hysteresis loops, magnetic force microscopy, and magnetostriction measurements. The chosen compositions cover an interval centered around 19–21 at. % where the best magnetostrictive response is supposed to be found. The samples were also submitted to thermal treatments and rapid cooling to promote the development of the A2 phase. The complementary information provided by these multiple techniques helps in clarifying the complex metastable Fe–Ga phase diagram in the studied Ga range and gives a comprehensive description of the phases present in the different alloys and of how they transform upon heating, making possible a direct relationship between microstructure and magnetic properties, magnetic domains configuration, and magnetostriction.

II. MATERIALS AND METHODS

Fe_{100-x}Ga_x, with $x = 18, 21, 23$ at. % Ga, master alloys were prepared by electric arc melting. Their composition was determined through semi-quantitative energy-dispersive x-ray spectroscopy (EDX) analysis on a SEM-FEG (FEI Inspect-F) using a standardless ZAF matrix correction routine. The samples were labeled as Ga18, Ga21, and Ga23, respectively. While EDX may not be very accurate, in our case the reported compositions matched well with those expected from saturation magnetization measurements (see Table III later in the text). In any case, the sample compositions were also checked using two additional independent methods.

For the first, selected portions of the three samples were dissolved using acid digestion in a microwave oven (Milestone MLS-1200 MEGA). Sample aliquots were treated with 5 ml of aqua regia in tetrafluoromethoxyl (TFM) bombs. Four heating steps of 5 min each (250, 400, 600, 250 W power, respectively), followed by a ventilation step of 25 min, were applied. At the end of the full treatment, the samples appeared completely dissolved. Subsequently, the resulting solutions were diluted to 20 ml with highly purified water. A further dilution (1:50) was necessary as a final step to determine Fe and Ga concentrations by inductively coupled plasma–optical emission spectroscopy (ICP-OES, Optima 7000 DV Perkin Elmer) equipped with a PEEK Mira Mist nebulizer, a cyclonic spray chamber, and an Echelle monochromator. The wavelengths were 238.204 and 417.206 nm for Fe and Ga, respectively. Each concentration value was averaged on the basis of

three instrumental measurements. Using this technique, the Ga content turned out to be 17.3 at. % for Ga18, 19.3 at. % for Ga21, and 20.9 at. % for Ga23 samples, respectively, therefore slightly poorer in Ga with respect to the composition determined by EDX.

For the second, atom probe tomography (APT) was used to investigate the redistribution of Ga in the Ga21 alloy. Two specimens for APT measurements were prepared by the standard electropolishing method^{27,28} using the Ethanol/Perchloric acid electrolyte in 75/25, 90/10, and 95/5-vol.%. The atom probe analyses were performed on a CAMECA LEAP 4000 HR, at 50 K, with a pulse fraction of 20% and a repetition rate of 200 kHz, with a detection rate of 0.15%. The data were processed using IVAS^{3.6.8} software.^{27,29} An example of the 3D reconstruction maps of the analyzed volumes for Ga (shown in purple) and Fe (shown in black) atoms is shown in Fig. 1. For both samples, three analyses have been conducted, and the Ga atoms were homogeneously distributed in the analyzed volume. The sample shown in Fig. 1 turned out to be constituted by 21.3 at. % of Ga, whereas the other sample contained 20.4 at. % of Ga, in excellent agreement with the composition determined by EDX and inductively coupled plasma–optical emission spectroscopy. For simplicity, the composition determined by EDX (Ga18, Ga21, and Ga23) will, therefore, be retained for the subsequent discussion.

The raw ingots had a typical size of the order of $6 \times 5 \times 4 \text{ cm}^3$ and were tempered in water. The cooling rate is known to significantly affect the microstructure,³⁰ but in ingots of this size it is extremely difficult to control the cooling rate and to ensure that it is homogeneous in the whole ingot volume. Therefore, in the case of the as-cast samples, a non-homogeneous microstructure is expected. The samples were cut with diamond wire to obtain parallelepiped-shaped samples $\approx 1 \text{ mm}$ thick. Finally, they were mirror-polished with diamond paste (final polish 0.25 μm). In order to promote both homogenization of the microstructure and phase transformations, selected samples for each composition were furnace annealed in vacuum (base pressure 1×10^{-6} mbar) at 1000 °C for 24 h, in a quartz tube. After the annealing, they were cooled to room temperature by removing the quartz tube from the furnace, ensuring an initial average cooling rate of ≈ 150 °/min down to 500 °C, followed by an average cooling rate of ≈ 40 °/min down to 300 °C. These cooling rates should be fast enough to minimize the development of the L1₂ phase at the expense of the D0₃ one.³¹

X-ray diffraction (XRD) analysis was conducted at room temperature with a Panalytical X'Pert Pro diffractometer in the Bragg–Brentano configuration (Cu radiation, $\lambda = 0.15418 \text{ nm}$) on polished samples. Since the XRD patterns of the A2, B2, and D0₃ phases were not available in the databases, the unit cells of the disordered and ordered phases of interest were built by means of the free software Vesta³² using space groups and lattice parameters data reported in Ref. 10 and their diffraction patterns calculated with the same software and used as a reference to index peaks in the experimental patterns.

Structural and magnetic phase transition temperatures were determined by differential scanning calorimetry (Pyris Diamond DSC, PerkinElmer) with a heating and cooling rate of 5 °C/min within a temperature range from 25 to 725 °C. The measurements were done under an Ar flow of approximately 20 ml/min. Each sample was subjected to two thermal cycles of heating and

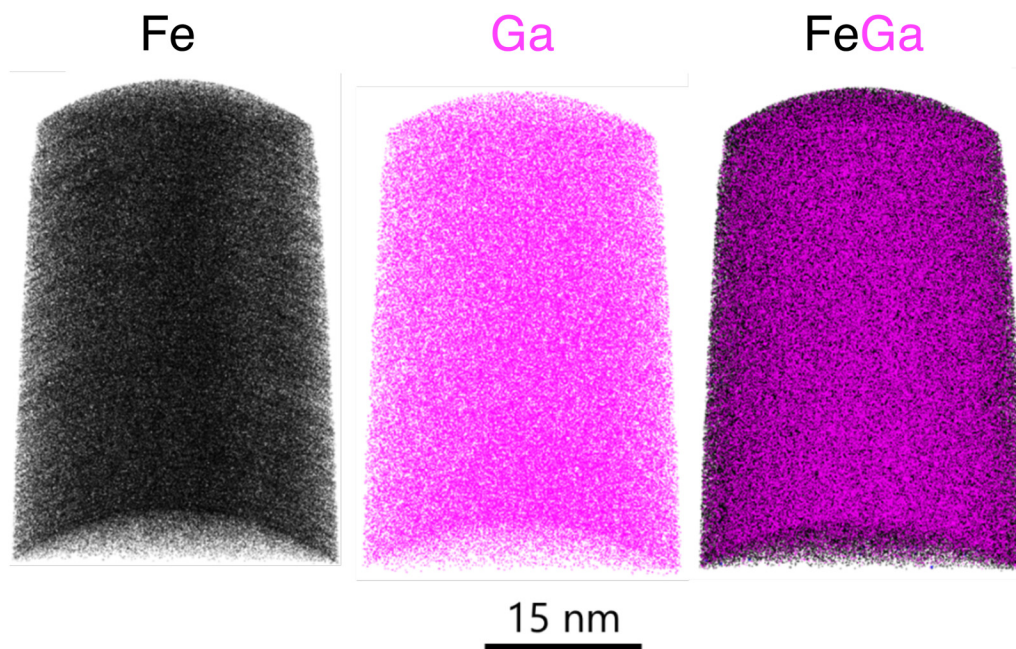


FIG. 1. 3D reconstruction of Ga (purple) and Fe (black) atoms in a Ga₂₁ sample volume analyzed by atom probe tomography.

cooling in order to distinguish reversible transformations (e.g., Curie transition, equilibrium phase transformations) from irreversible ones (e.g., metastable phase transformations). The heat flux of the empty copper crucible recorded in the same measurement conditions was subtracted from the heat flux of each sample to get rid of the baseline contribution to the measured signal, due to instrumental factors and to a slight oxidation of the copper itself.

Mössbauer Spectroscopy, performed at room temperature, was also exploited to identify the different phases present in the samples by properly evaluating the parameters resulting from the hyperfine interaction (the hyperfine field B_{hf} and the isomer shift δ). The CEMS technique (Conversion Electron Mössbauer Spectroscopy) has a penetration depth of about 80–100 nm and is, therefore, useful for analyzing the near surface region^{33,34} of the samples. CEMS experiments were performed at room temperature and in normal incidence by using a He-CH₄ gas flow proportional counter.³⁵ The radioactive source was ⁵⁷Co in a rhodium matrix with an activity of ≈ 1.5 GBq, moved in constant acceleration mode. Magnetic CEMS spectra were fitted with a discrete distribution of hyperfine fields B_{hf} with a least-squares procedure.³⁶ A correlation between hyperfine field and isomer shift δ was used to take into account the Fe environment distribution.^{37–40} δ values at the ⁵⁷Fe nuclei are given relative to α -Fe at room temperature. Estimated errors for the hyperfine parameters originate from the statistical errors σ given by the fitting program, taking a confidence value of 3 (i.e., 3σ).

For magnetic characterizations, the samples were cut into approximately $2 \times 2 \times 1$ mm³ pieces to be fitted into a vibrating sample magnetometer (VSM, LakeShore 7410). Hysteresis loops were measured at room temperature, whereas magnetization vs

temperature was measured up to 680 °C under an applied field of 500 Oe (50 mT). Saturation M_S , remanence M_r , and coercivity H_c have been extracted from hysteresis loops data, whereas Curie temperatures T_C were obtained from temperature-dependent curves.

Additional magnetic characterizations were performed by magnetic force microscopy (MFM, Bruker Multimode V) exploiting Co-Cr coated Si tips (Bruker MESP-HR) in intermittent-contact lift mode with a typical lift scan height of 50 nm. The tips were magnetized along their axis. The samples were analyzed by MFM at their in-plane magnetic remanence state. In the MFM, in addition to the height channel (AFM), the magnetic information was obtained through the phase channel in pass 2.

The samples used for magnetostriction measurements were cut into pieces having a size of $\approx 10 \times 6 \times 1$ mm³. Strain gauges with a resistance of $\approx 120 \Omega$ were glued with epoxy resin on the samples surface, and the measurements were made at room temperature by a Wheatstone bridge under an applied magnetic field aligned along the 6 mm side of the sample. The measurements were performed by aligning a saturating magnetic field (10 kOe = 1 T) along the 6 mm edge, then by rotating the sample by 90° under the same saturating field (now aligned to the 10 mm side). The value $\Delta\lambda$ representing the difference of the reading of the strain gauge in the two configurations allows one to calculate the saturation magnetostriction value according to the expression $\lambda_s = \frac{2}{3}\Delta\lambda$.⁴¹

III. RESULTS AND DISCUSSION

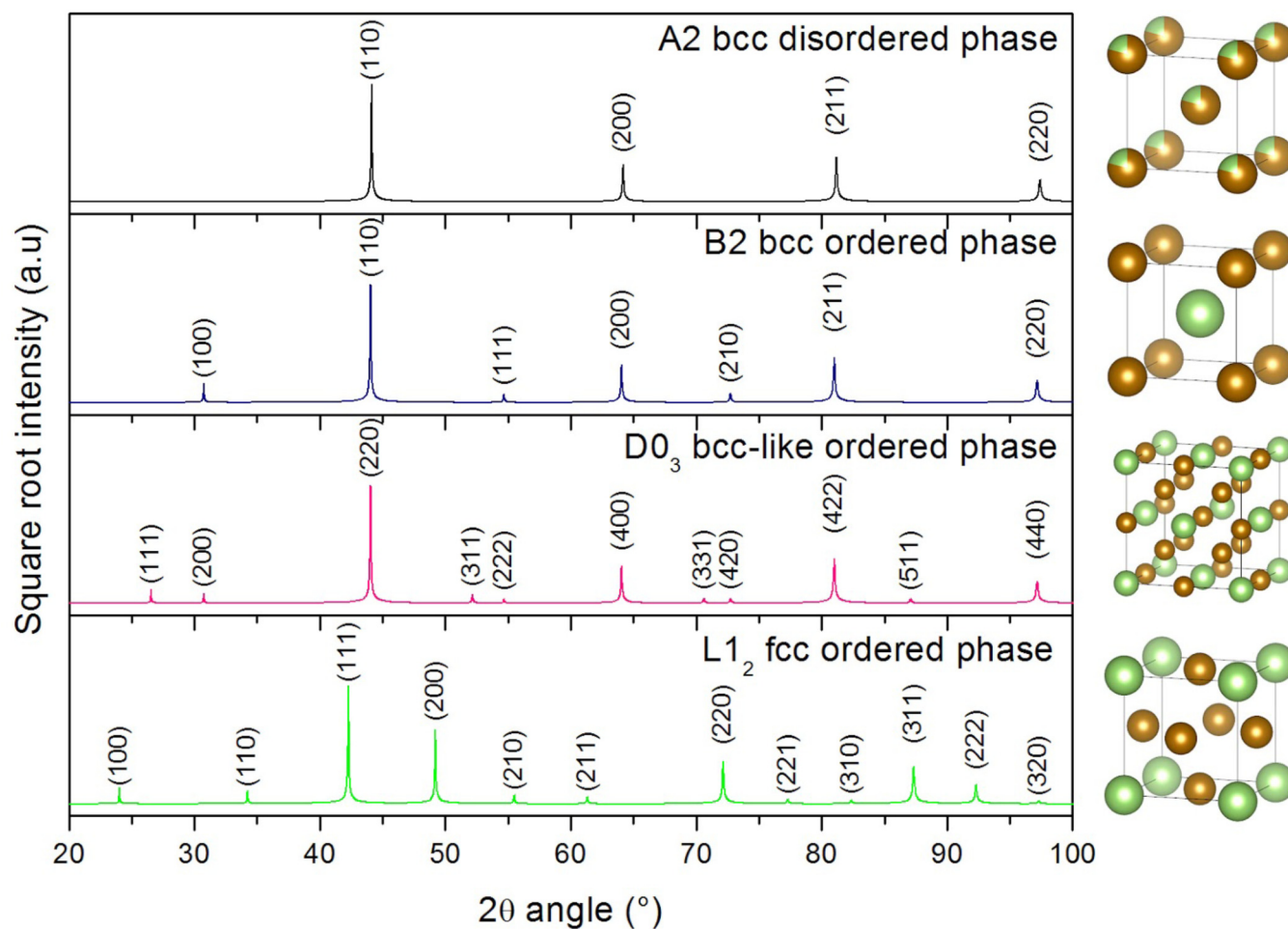
In the region the phase diagram⁹ relevant for the present study, i.e., the portion with the Ga content within 18 and 23 at. %, 05 JULY 2023 13:44:34

the equilibrium phases are the A2 disordered bcc structure and the $L1_2$ fcc superlattice. However, the bcc-ordered phases B2 and $D0_3$ can be quenched at room temperature due to the slow kinetics of phase transformation.^{9,30} As a matter of fact, several authors^{24,30} report that as cast Fe–Ga alloys usually present a metastable structure, dependent on the Ga content: for Ga < 20% only the A2 phase is present, whereas for Ga between 20 and 27% $D0_3$ clusters of increasing size³⁰ are observed embedded in the A2 matrix.

The identification of ordered and disordered FeGa phases through standard laboratory x-ray diffraction is a difficult task, since the superlattice lines, produced by atomic ordering, are very weak and difficult to detect since Fe and Ga have a similar atomic number ($Z=26$ and 31 , respectively) and hence similar scattering factors.^{26,42} In addition, the fundamental lines of bcc-derived phases appear at very similar angular positions since the atomic ordering does not

produce appreciable changes in lattice parameters. Peak splitting of high angle reflections [e.g., (220)] has been used in addition to superlattice lines as a tool to detect two-phase mixtures of A2 and $D0_3$;⁴³ however, this approach requires high resolution diffractometers and small peak FWHM. Figure 2 shows the calculated XRD patterns of the disordered A2 phase and of the three ordered phases of interest (B2, $D0_3$, and $L1_2$). The patterns were generated by building the unit cells of each phase (displayed on the right of Fig. 2) with Vesta free software³² using the lattice parameters reported in Ref. 10 for the following compositions: $Fe_{80}Ga_{20}$ (A2), $Fe_{75}Ga_{25}$ ($D0_3$ and $L1_2$), and $Fe_{61}Ga_{39}$ (B2). As one can see, the patterns of all the bcc phases are very similar, differing only for the presence of low intensity reflections due to atomic ordering in a superlattice.

X-ray diffractograms of the as-prepared and annealed samples are reported in Fig. 3. The Ga18 sample is essentially a single phase



05 July 2023 13:44:34

FIG. 2. Comparison of calculated XRD patterns of the ordered and disordered phases in the Fe-rich region of the Fe–Ga phase diagram ($\lambda = 1.54059 \text{ \AA}$). The square root of intensities is presented to better display the low-intensity superlattice reflections due to atomic ordering. The unit cell of each phase is represented on the right (not-to-scale). Green spheres represent Ga atoms, brown spheres Fe atoms, while double-colored spheres represent positions where either Fe or Ga atoms can be present.

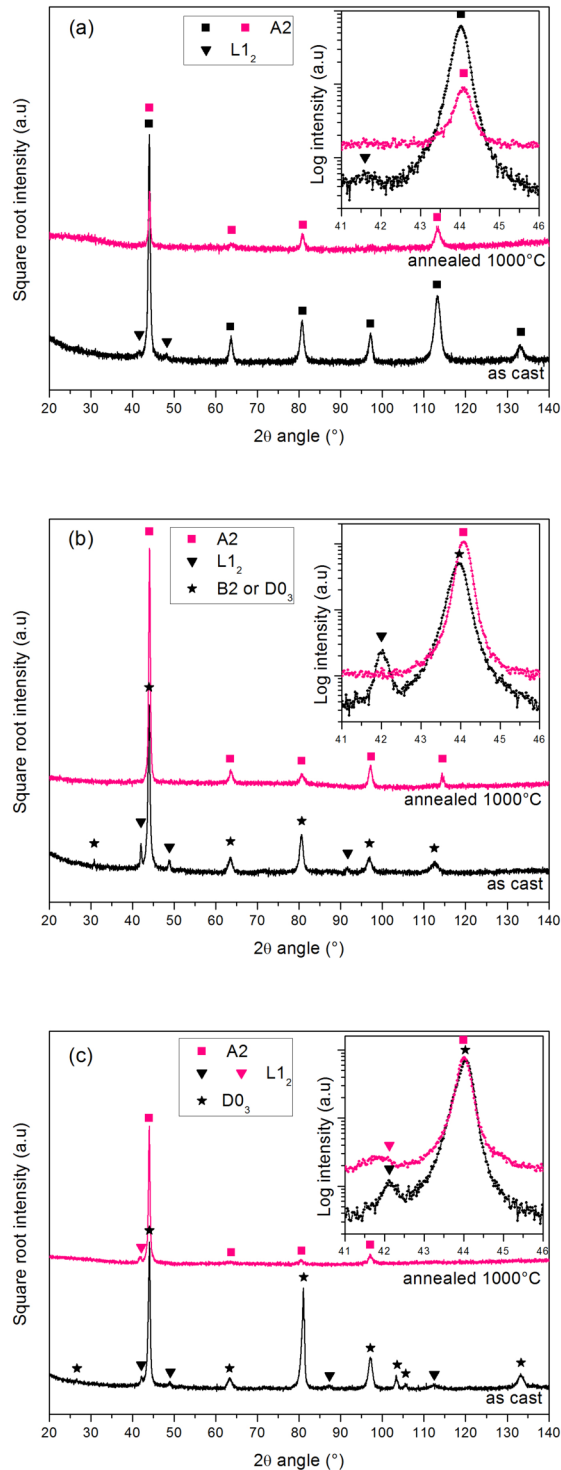


FIG. 3. Diffractograms of the $x = 18$ (a), 21 (b), and 23 (c) at. % Ga samples, as-cast and annealed. Patterns have been vertically translated for a better evaluation of the details.

material with an A2 disordered structure. In this sample, only minimal traces of peaks attributable to $L1_2$ phase are visible. After the heat treatment at 1000°C , no substantial change in peak positions of the A2 phase has been observed. On the other hand, the minor peaks of $L1_2$ were not detected, although they might have been missed owing to the lower overall intensity of the annealed sample pattern due to the reduced sample size of the annealed specimen. In the XRD pattern of the as-cast Ga21 sample, a weak superlattice line is visible at low angles, revealing that this sample may contain a certain proportion of ordered bcc phase (either B2 or $D0_3$) embedded in the A2 matrix, together with the $L1_2$ fcc ordered phase. After annealing at 1000°C , both the superlattice lines and the $L1_2$ peaks disappeared, leaving a single phase material with peaks shifted toward higher angles, indicating a decrease in lattice parameter of the cell possibly due to a phase transformation from $D0_3$ /B2 structure to A2 structure.⁴³ The main peaks of sample Ga23 are well matched by the reflections of the $D0_3$ ordered phase, since, in addition to a weak superlattice line at low angle, other lines unique to this phase are visible around $2\theta \approx 105^\circ$. The appearance of these reflections at high angle and, more generally, the deviations of relative intensities from the ones expected for a random powder, observed in all the samples, are likely due to the coarse grain size of the alloy ($400\text{--}700\mu\text{m}$), that causes only a few crystals to diffract, especially at high angles. As in previously described samples, the disordered A2 phase cannot be excluded: indeed, at a closer inspection, the peaks of the fundamental lines appear quite asymmetrical with a shoulder on the low angle side of the profile, possibly revealing the coexistence of different phases with the same crystal structure but slight differences in lattice parameters. Upon annealing, the reflections of the $D0_3$ phase disappear. In addition, the peaks of the $L1_2$ phase are detectable both in the as-cast and in the annealed state.

In general, therefore, the studied samples in the as-cast state follow the behavior already observed by other studies,²⁶ where faint superlattice lines were observed starting for alloys with Ga at. % greater than 21%,⁴⁴ revealing that the out-of-equilibrium solidification conditions were able to quench a certain amount of the ordered phase stable at temperatures $>588^\circ\text{C}$, whereas after annealing, the $D0_3$ phase, when present in the as-cast samples, transforms into the A2 one, eventually disappearing as expected owing to its metastability at room temperature.

Mössbauer spectroscopy (Fig. 4) gives a direct link between the samples crystal structure and their magnetic properties, as it is sensitive to the environment in which the Fe atoms are placed. All spectra reported in Fig. 4 for the as-prepared samples display a sextet, typical of ferromagnetic behavior, with relatively large peaks, suggesting a disordered crystal structure, which evolves into a slightly more ordered one (narrower peaks) as the Ga content is increased. All three compositions show a peak of the hyperfine field distribution around 300 kOe (30 T), attributed to a Fe-rich phase. As the width of the peak is rather large, this phase must be disordered; therefore, this peak can be assigned to the A2 phase. The fit was improved by adding a paramagnetic quadrupolar doublet with a quadrupole splitting value of about 1.2 mm/s, assigned to a minority phase, not detected by XRD. The relative spectral area of this paramagnetic minor phase increases with Ga content. This paramagnetic contribution is attributed to a Ga-rich phase. The average hyperfine field

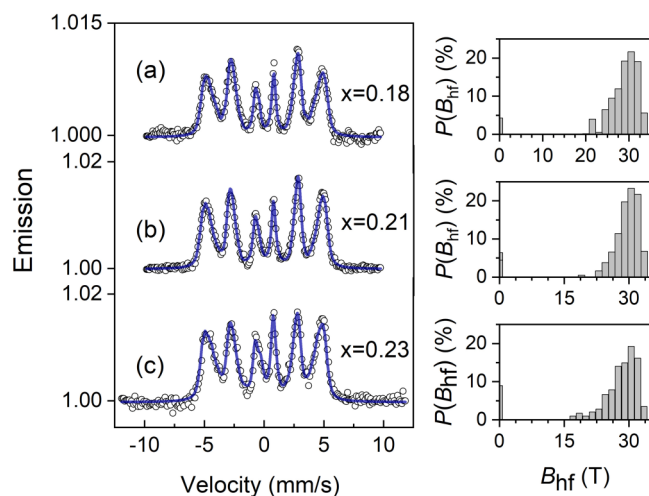


FIG. 4. CEMS spectra at room temperature and the corresponding hyperfine field distributions of the Ga18 (a), Ga21 (b), and Ga23 (c) alloys.

value decreases with Ga content, as reported in Table I and in agreement with the literature.⁴⁵ Average values of the isomer shifts do not show a significant variation within this small range of compositions. However, the highest value of $\langle \delta \rangle$ is obtained for the Ga23 sample, in agreement with an increase in isomer shift with Ga content reported in the literature.^{45,46}

Complementary information comes from differential scanning calorimetry, which is able to detect phase transformations occurring as a function of temperature. Table II lists the magnetic and structural transformations possible in the Fe–Ga alloys of selected compositions, whereas Fig. 5(a) displays the DSC traces of the as-cast samples. For each sample, the first heating and first cooling curves are reported to evaluate the reversibility of the observed signals. The signal derivatives are reported in panel (b) to better detect the small changes observed mainly in a region of rapid variation of the baseline signal. For sample Ga18, only the FM \rightarrow PM transition [t18-1] is expected within the temperature range of the DSC (see Table II); as a matter of fact, there are no significant features highlighted by the DSC curve, considering that even its derivative signal is completely flat in the high temperature region shown in Fig. 5(b): this is in agreement with XRD data, since this sample is mainly composed of stable phases (A2 and L₁₂). As a general rule, the Curie temperatures of all Fe–Ga magnetic phases decrease

with increasing Ga content, with a steep decrease in the range of Ga 15–25 at.%.⁴⁵ An increase in the Curie temperature could appear only if large amounts of the L₁₂ phase were present, which is not our case. According to the available literature data,⁹ the A2 phase should have a Curie temperature within the DSC measurement range for Ga > 18 at.%. However, since the heat capacity change associated with magnetic transitions is very small (roughly 0.1 Jg⁻¹ °C⁻¹),⁴⁷ Curie temperature is often missed by conventional DSC measurements, because its signal can be lost in baseline curvature and related DSC cell effects. Samples Ga21 and Ga23, instead, display a richer set of possible transformations upon heating (see Table II) and show clear peaks in the high temperature range of the DSC measurement, especially evident in the cooling curves, thus related to reversible phenomena. However, the exact attribution of the observed signals to a particular physical process is difficult, owing to the complexity of the multiphase system and to the subtle differences between the phases.

In the DSC traces of sample Ga21, only two of the five predicted events are detected: the heating curve has extremely faint variations in the steep descendent portion, but looking at the derivative two minima are apparent, that seem to indicate two distinct processes occurring at close, but different temperatures: namely, 645 and 660 °C. This is qualitatively consistent with the observed thermomagnetic behavior, although temperature differences are observed between calorimetric and magnetic data for the event at lower temperature. The same features have been observed in the second heating and second cooling runs (not shown) as well, indicating a fully reversible thermal behavior.

Ikeda *et al.*⁹ have performed DSC experiments on Fe–Ga alloys of a composition (Ga 21.5 at.%) similar to ours: they observed three signals that were attributed to processes [t21-1], [t21-2], and [t21-4] mentioned in Table II, although the signal of process [t21-1] was quite faint and they did not consider the possible transformations of L₁₂ phase that was also present in their samples. In our case, even if the D₀₃ quenched phase is present in this sample, we may have missed its magnetic transition in DSC measurements owing to the baseline curvature in that temperature region. On the contrary, the D₀₃ FM \rightarrow PM transition was evident in the $M(T)$ curve, as we will discuss later. We assume that the processes detected by calorimetric measurements in Ga21 are [t21-2] and [t21-4].

DSC curves of sample Ga23 show a peak easily detected in the heating and cooling traces; the signal derivatives do not reveal additional peaks, although the signal in the high temperature portion of the derivative is quite broad and may represent convoluted processes. These processes occur at the highest temperature among the studied samples; this is consistent with the phase diagram, since on increasing Ga content the temperature of the order–disorder transformation increases, while the T_c of the A2 phase decreases, thus making processes [t21-2] and [t21-4] progressively closer until they practically coincide for $x = 22.8\%$ (see Table II). So, the signal observed in the DSC trace of Ga23 may be associated with an order–disorder transformation occurring between paramagnetic phases that will not be detected by thermomagnetic measurements.

The phase transformations occurring during annealing have, therefore, also been observed by means of magnetization vs temperature measurements, under an applied field of 500 Oe (50 mT),

TABLE I. Average values of hyperfine field $\langle B_{hf} \rangle$, isomer shifts $\langle \delta \rangle$, and spectral area A_p of the paramagnetic phase, deduced from the fit of the Mössbauer data of the Ga18, Ga21, and Ga23 as-prepared samples.

Ga (%)	$\langle B_{hf} \rangle$ (kOe)	$\langle B_{hf} \rangle$ (T)	$\langle \delta \rangle$ (mm/s)	A_p (%)
18	281	28.1	0.19(3)	4
21	279	27.9	0.18(7)	6
23	258	25.8	0.20(3)	9

TABLE II. List of magnetic and structural transformations for the selected compositions of Fe–Ga alloys. Transformations are listed in each column in order of increasing temperature, and labeled with an identification code [in square brackets] used as a reference in the text. FM indicates ferromagnetic phases; PM indicates paramagnetic phases; q postfix indicates a quenched, metastable phase.

Sample	Ga 18 at. %	Ga 21 at. %	Ga 23 at. %
Phase composition from XRD	A2	$D0_3q + L2_1$	$D0_3 + L2_1$
Transformations	A2 FM \rightarrow A2 PM $T \approx 690^\circ\text{C}$ [t18-1] magnetic transition	$D0_3q$ FM \rightarrow $D0_3q$ PM $T = 536^\circ\text{C}$ [t21-1] magnetic transition $D0_3$ PM \rightarrow A2 FM $T \approx 600^\circ\text{C}$ [t21-2] order-disorder $L1_2 + D0_3 \rightarrow D0_{19}$ $T = 605^\circ\text{C}$ [t21-3] reverse eutectoid A2 FM \rightarrow A2 PM $T \approx 670^\circ\text{C}$ [21-4] magnetic transition $D0_{19} \rightarrow B2$ $T = 680^\circ\text{C}$ [t21-5] congruent reaction	$D0_3q$ FM \rightarrow $D0_3q$ PM $T \approx 520^\circ\text{C}$ [t23-1] magnetic transition $L1_2 + D0_3 \rightarrow D0_{19}$ $T = 605^\circ\text{C}$ [t23-2] reverse eutectoid $D0_3$ PM \rightarrow A2 PM $T \approx 650^\circ\text{C}$ [t23-3] order-disorder $D0_{19} \rightarrow B2$ $T = 680^\circ\text{C}$ [t23-4] congruent reaction

reported in Fig. 6. All three samples are ferromagnetic at room temperature, and their magnetization initially increases slightly with temperature because of the progressive increase in the magnetic permeability at the applied field value when the temperature is increased: in fact, at 500 Oe (50 mT), the samples are not saturated. Then, all samples display one or more processes where their magnetization drops, which mark the Curie temperatures of the crystalline phases present in the samples. For the Ga18 specimen, there is one huge drop of the magnetization at $\approx 690^\circ\text{C}$,^{24,48}

whereas for the Ga21 and Ga23 samples minor drops of the magnetization at ≈ 530 and $\approx 400^\circ\text{C}$, respectively, are observed before the last drop at ≈ 660 and 490°C , respectively, indicating the presence of a minority phase whose Curie temperature is lower. For the Ga21 sample, after the first magnetization drop with temperature, a subsequent increase is observed, clearly indicating that the phase having the lower Curie temperature is transforming into the one with the higher T_c .²⁰ This could be the case for the Ga23 sample as well, but the amount of the minority phase is so small that it

05 JULY 2023 13:44:34

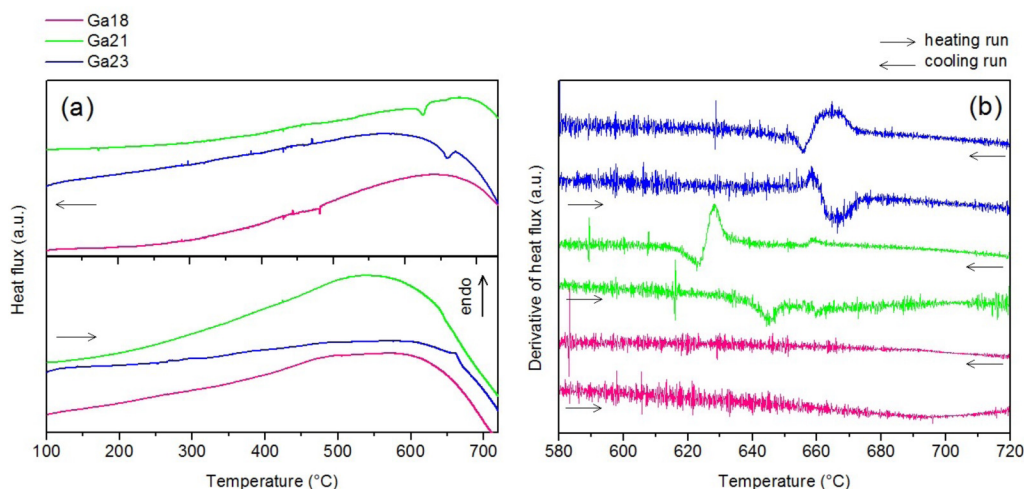


FIG. 5. DSC traces of the studied samples recorded with a temperature rate of $5^\circ\text{C}/\text{min}$. (a) Heat flux of the first heating and first cooling segments of the measurement (the arrow represents the direction of the temperature ramp). (b) Signal derivatives in a reduced temperature range. The colors identify the samples in the same way in both graphs. The curves have been vertically translated for clarity.

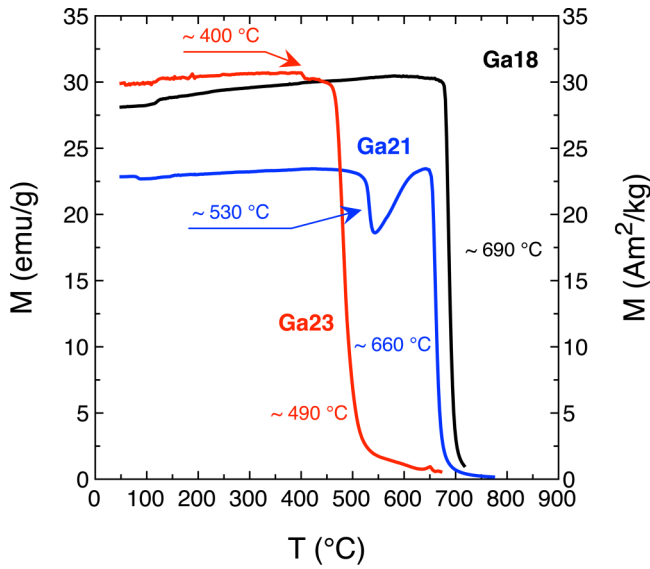


FIG. 6. Magnetization as a function of temperature on the Ga18, Ga21, and Ga23 samples, measured under an applied magnetic field of 500 Oe.

weakly contributes to the magnetization signal. The Curie temperatures extracted from the curves in Fig. 6 are also reported in the figure: they are in excellent agreement with the values reported in the literature for similar compositions.¹¹

For the Ga18 sample, the $T_c \approx 690^\circ\text{C}$ perfectly matches with the Curie temperature of the A2 phase,^{9,12,49} that is indeed the dominating one as detected by XRD and Mössbauer ([t18-1], see Table II). No phase transformations are detected during heating, in agreement with XRD and DSC data. For the Ga21 sample, the first Curie temperature at $\approx 530^\circ\text{C}$ matches very well with the FM \rightarrow PM D₀₃ transition [t21-1],⁹ as also confirmed by XRD. Then, the paramagnetic D₀₃ phase transforms into the A2 one

[t21-2], giving rise to the increase in the magnetic signal at $\approx 600^\circ\text{C}$ in Fig. 6, that will eventually reach its Curie temperature, slightly decreased to $\approx 660^\circ\text{C}$ ²⁰ and in excellent agreement with DSC data [t21-4]. Finally, the Ga23 sample displays a first event at approximately 400°C , which probably marks the overlapping occurrence of the ferromagnetic to paramagnetic transition of the D₀₃ phase [t23-1],^{9,20} and the transformation of the D₀₃ phase into the A2 one, still ferromagnetic. Finally, the drop of the magnetization at $T_c \approx 490^\circ\text{C}$ marks the Curie temperature of the resulting A2 phase: in fact, the progressive decrease of the Curie temperatures of all phases in the annealed samples is due to the decrease in the average magnetic moment per Fe atom as Ga content increases.^{11,45}

The effect of annealing on the magnetic properties of the Fe-Ga alloys is shown in Fig. 7. All hysteresis loops display soft magnetic behavior, with a low-field slope that is due to the demagnetizing field arising from the sample geometry and the open magnetic circuit measurement configuration [Fig. 7(c)]. The accurate determination of the coercive field through VSM is difficult, as H_c is of the order of the Oe [Fig. 7(b)], therefore of the same order of the applied field step. With an increase in Ga content, the saturation magnetization decreases [Fig. 7(a)], in perfect agreement with the literature^{11,45} (see Table III). Annealing at 1000°C for 24 h induces the phase transformations that have been investigated through XRD, DSC, and Mössbauer techniques: the overall increase in the disordered A2 phase at the expense of the ordered D₀₃ one is accompanied by a slight increase in the saturation magnetization.¹¹

Representative images of the surface magnetic domain configurations at the magnetic remanence for all the as-cast and annealed samples, acquired by magnetic force microscopy, are shown in Fig. 8. Since the crystals size, as observed from electron microscopy (data not shown here), is in the $400\text{--}700\ \mu\text{m}$ range for all samples, the images in Fig. 8 cover individual grains, except for the presence of small inclusions or precipitates that could have a narrow and long shape. As a function of the Ga content, and also before and after annealing, there are strong variations of the domains configuration that are a consequence of the different phases present in the

05 JULY 2023 13:44:34

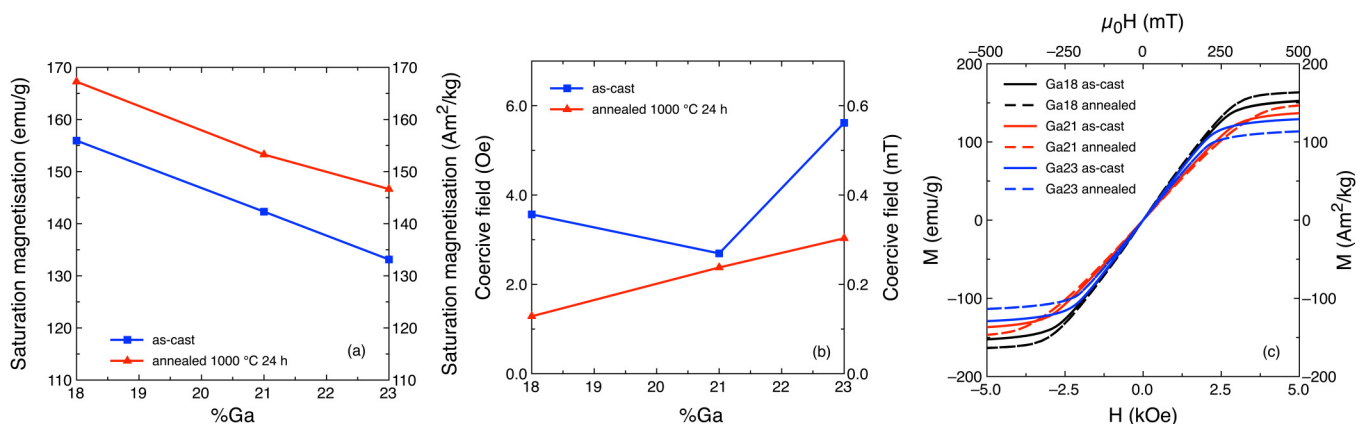


FIG. 7. (a) Evolution of the saturation magnetization with Ga content for the as-cast and annealed (1000°C 24 h) samples. (b) The same for the coercive field. (c) Room temperature hysteresis loops of the Ga18, Ga21, and Ga23 samples, as-cast and annealed 1000°C 24 h.

TABLE III. Saturation magnetization M_S as a function of Ga content. Values marked with an asterisk * are taken from Ref. 45; values marked with a double asterisk ** are taken from Ref. 11 and rescaled to 298 K by assuming a Langevin-type dependence of the saturation magnetization with the T/T_C ratio.

Ga%	M_S (emu/g) or (Am^2/kg)
0	220*
5	210*
10	195*
18	156
18	159**
20	160*
20	153**
21	142
23	133
23	131**
25	130*

samples. The Ga18 sample in the as-cast state is characterized by stripe domains, with irregular borders, more or less aligned along a common direction, that according to Ref. 8 is the local [100] direction of the A2 crystal. The irregular borders are sometimes

associated with the presence of precipitates in the A2 phase.⁵⁰ Our XRD data confirm the presence of traces of the $L1_2$ phase in the predominant A2 matrix. After annealing, the irregularities on the stripes borders become so pronounced that a domain configuration starting to resemble a dendritic one appears. The presence of such features is commonly attributed to the presence of $D0_3$ or other precipitates in the A2 matrix;^{8,51} however, in our case XRD data do not reveal any significant changes in the crystal structure of the annealed sample with respect to the as-cast one; therefore, this explanation must be ruled out. However, it is important to remark that the Ga18 samples display the largest magnetostriction (see below). As it has been pointed out in Refs. 52 and 53, the polishing process required to prepare the samples surface for the MFM investigations can induce an additional anisotropy term, possibly competing with the crystalline one. The MFM images reported in Figs. 8(a) and 8(b) may therefore display artifacts: the dendrites or stripes with irregular borders might only appear at the surface and not be representative of the bulk domain structure.

The as-cast Ga21 sample is characterized by a disordered magnetic configuration, with regions having a decreased contrast. Indeed, this sample consists of B2 or $D0_3$ phases, the latter along with a higher amount of the $L1_2$ phase are possibly responsible for the low-contrast areas.^{13,51} After annealing, the present phases

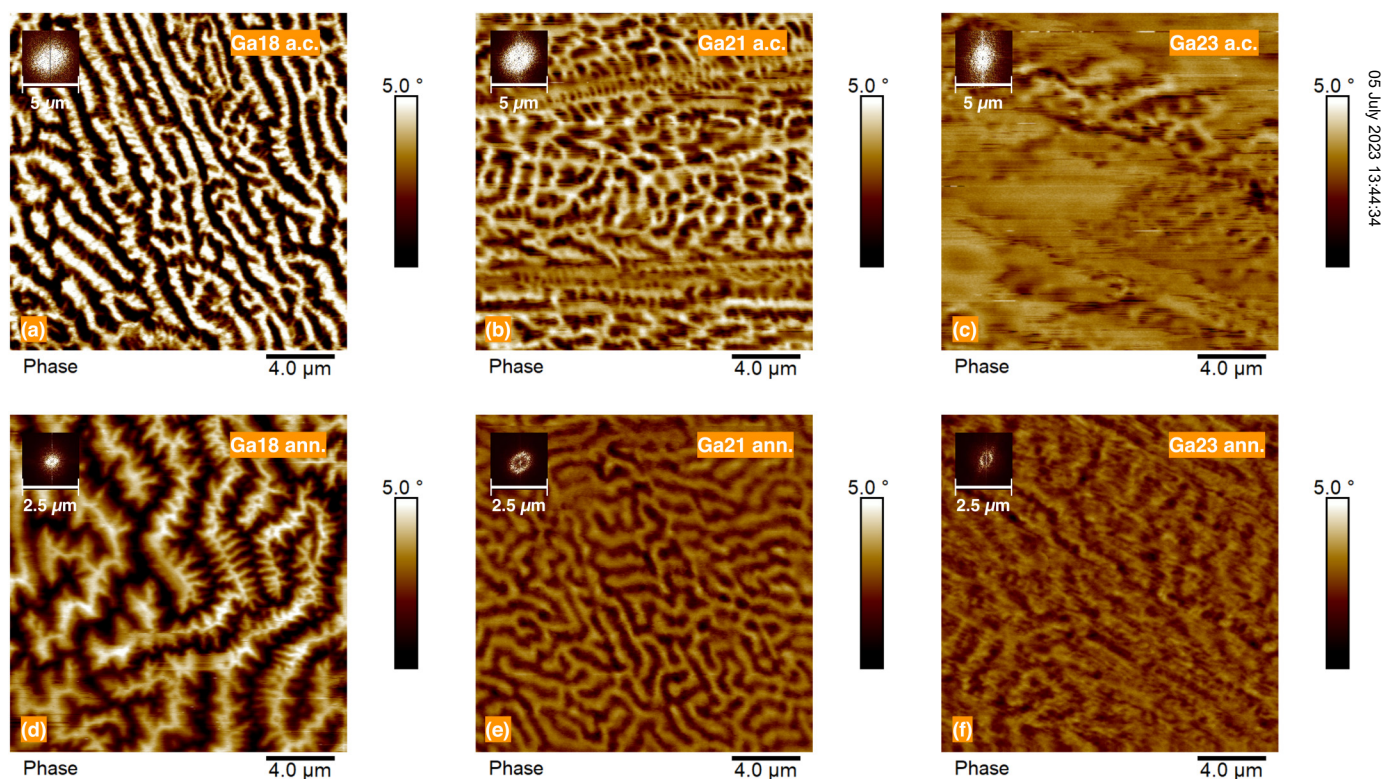


FIG. 8. MFM images at the magnetic remanence of Ga18, Ga21, and Ga23 samples in the as-cast [a.c., panels (a), (b), and (c), respectively] and annealed [ann., panels (d), (e), and (f), respectively] states. In the insets, FFT transforms of the same images.

transform into the A2 one, according to XRD and M vs T measurements, giving rise to the maze- or stripe-domain structure (for the same reasons as discussed for the Ga18 sample).

The Ga23 sample in the as-cast state, instead, is mostly constituted by the $D0_3$ phase, according to XRD data. This results in a very weak magnetic contrast, with large domains,¹³ with small regions displaying some very disordered maze- or stripe-domains, that can be attributed to the possibly present A2 phase. After annealing, a domain configuration similar to the one of the Ga21 annealed sample develops, although with more irregular borders, compatible with the co-presence of the A2 phase with $L1_2$ precipitates, in agreement with XRD data.

All MFM images reported in Fig. 8 have also been analyzed by 2D-FFT, the respective results appearing in the insets. The FFTs provide a visual indication of the degree of order (or disorder) of the magnetic domain configuration of the corresponding samples. All three as-cast alloys are characterized by FFT images consisting of large halos, indicating that there is no long-range order in the domains configuration. The same applies to the Ga18 annealed sample, that even though has a slightly different domain pattern, does not display a significant evolution of its structure, as discussed earlier. Conversely, the Ga21 and Ga23 annealed samples show FFT images consisting of rings, indicating that there is a certain degree of order in the magnetic domains configuration, although isotropic, with typical features size of the order of 500 nm.

The saturation magnetostriction results are reported in Fig. 9, as a function of Ga content, for both the as-cast and annealed samples. It is important to remark that the samples are polycrystalline with non oriented grains, therefore inducing magnetostrictive

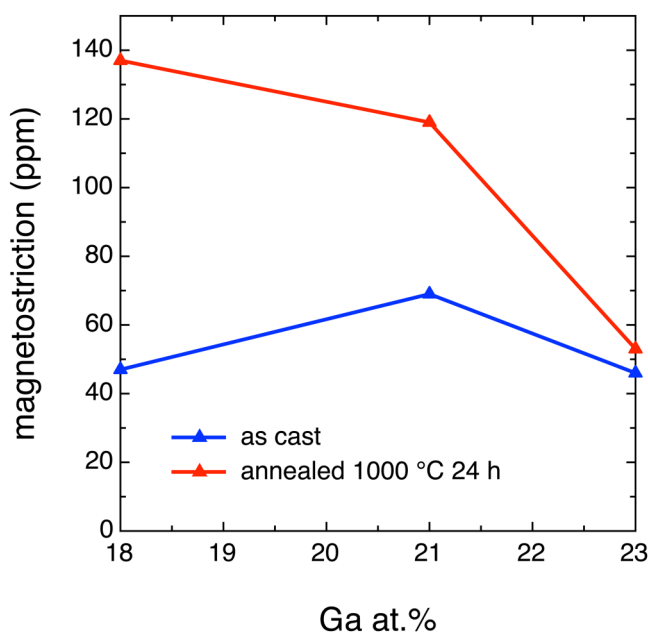


FIG. 9. Ga content dependence of the saturation magnetostriction for the as-cast and annealed (1000 °C 24 h) samples.

responses quite different from single-crystal samples.⁵⁴ The as-cast samples are characterized by lower values of magnetostriction, oscillating between 50 and 60 ppm (parts-per-million) as a function of the Ga content. The presence of the $D0_3$ phase at least in the as-cast Ga21 and Ga23 samples might affect this relatively low value of magnetostriction.^{8,51} After annealing, a significant increase in the saturation magnetostriction is observed for Ga18 and Ga21 samples due to the transformation of the $D0_3$ phase into the A2 one.⁸ The large increase in the saturation magnetostriction in the annealed Ga18 sample with respect to the as-cast one is noteworthy: its larger domains size should indeed favor a better magnetostrictive response,⁵¹ even though apparently the domains are less aligned along a common direction. The progressive reduction of the magnetostriction, in the annealed samples, with the Ga content, instead, is expected in this range of compositions.⁸

IV. CONCLUSIONS

Fe–Ga alloys were prepared in bulk form with compositions equal to 18, 21, and 23 Ga at. %. While all three alloys already display a moderate magnetostriction in their as-cast state, annealing at 1000 °C for 24 h significantly improves the magnetostrictive response. The combined use of multiple techniques, such as x-ray diffraction, Mössbauer spectroscopy, differential scanning calorimetry, temperature-dependent magnetization curves, and magnetic force microscopy, allowed to assess the structure–property relationships in the studied alloys and to evaluate the transformations occurring during annealing. As Ga content is increased, the disordered A2 phase is accompanied by the ordered $D0_3$ one, which is, however, detrimental to the development of the magnetostriction. With the high-temperature annealing and the subsequent rapid cooling, the $D0_3$ phase transforms into the A2 one. Even if the hysteresis loop properties are not significantly affected, apart from a $\approx 5\%$ – 6% increase in the saturation magnetization, the phase transformations imply profound changes in the magnetic properties, affecting the magnetic domains and the magnetostriction: the best performance is obtained with compositions close to 19%: in our case, the alloy having 18 at. % of gallium reached almost 240 ppm of saturation magnetostriction after annealing.

With this study, we have contributed to clarifying the out-of-equilibrium Fe–Ga phase diagram in the 18–23 Ga at. %, and the phase transformations occurring with temperature, affecting the magnetic and magnetostriction properties of the alloy.

ACKNOWLEDGMENTS

This work has been partially performed at NanoFacility Piemonte, an INRIM laboratory supported by Compagnia di San Paolo Foundation. The authors would like to thank Professor Frédéric Danoix for providing the samples, which were elaborated at the ARCELOR company.

AUTHOR DECLARATIONS

Conflict of Interest

The authors have no conflicts to disclose.

05 July 2023 13:44:34

Author Contributions

Marco Coisson: Conceptualization (equal); Investigation (lead); Methodology (equal); Visualization (lead); Writing – original draft (lead); Writing – review & editing (lead). **Kouassi Dakmak N'Dri:** Investigation (supporting); Writing – original draft (supporting); Writing – review & editing (supporting). **Lindor Diallo:** Investigation (supporting); Writing – original draft (supporting); Writing – review & editing (supporting). **Elena S. Olivetti:** Investigation (equal); Writing – original draft (equal); Writing – review & editing (equal). **Luca Martino:** Investigation (supporting). **Carlo P. Sasso:** Investigation (equal); Methodology (equal). **Federica Celegato:** Investigation (equal); Writing – review & editing (equal). **Gabriele Barrera:** Methodology (equal); Writing – original draft (equal); Writing – review & editing (equal). **Massimo Pasquale:** Methodology (equal); Writing – original draft (equal); Writing – review & editing (equal). **Paola Rizzi:** Investigation (supporting). **Mery Malandrino:** Investigation (equal). **Olha Nakonechna:** Investigation (equal). **Fabien Cuvilly:** Investigation (equal). **Paola Tiberto:** Conceptualization (equal); Writing – review & editing (equal). **Jean Juraszek:** Investigation (equal); Methodology (equal). **Saida Bahamida:** Writing – review & editing (equal). **Abdeslem Fnidiki:** Conceptualization (equal); Methodology (equal); Writing – original draft (equal); Writing – review & editing (equal).

DATA AVAILABILITY

The data that support the findings of this study are available from the corresponding author upon reasonable request.

REFERENCES

- D. E. Parkes, L. R. Shelford, P. Wadley, V. Holý, M. Wang, A. T. Hindmarch, G. van der Laan, R. P. Champion, K. W. Edmonds, S. A. Cavill, and A. W. Rushforth, "Magnetostriptive thin films for microwave spintronics," *Sci. Rep.* **3**, 2220 (2013).
- T. Ueno, C. Saito, N. Imaizumi, and T. Higuchi, "Miniature spherical motor using iron-gallium alloy (galfenol)," *Sens. Actuators, A* **154**, 92–96 (2009).
- T.-D. Onuda, Y. Wang, C. J. Long, and I. Takeuchi, "Energy harvesting properties of all-thin-film multiferroic cantilevers," *Appl. Phys. Lett.* **99**, 203506 (2011).
- J.-M. Hu, Z. Li, L.-Q. Chen, and C.-W. Nan, "High-density magnetoresistive random access memory operating at ultralow voltage at room temperature," *Nat. Commun.* **2**, 553 (2011).
- H. Ahmad, J. Atulasimha, and S. Bandyopadhyay, "Reversible strain-induced magnetisation switching in FeGa nanomagnets: Pathway to a rewritable, non-volatile, non-toggle, extremely low energy straintronic memory," *Sci. Rep.* **5**, 18264 (2016).
- D. C. Jiles, "The development of highly magnetostriptive rare earth-iron alloys," *J. Phys. D: Appl. Phys.* **27**, 1–11 (1994).
- J. Atulasimha and A. B. Flatau, "A review of magnetostriptive iron-gallium alloys," *Smart Mater. Struct.* **20**, 043001 (2011).
- F. Bai, J. Li, D. Viehland, D. Wu, and T. A. Lograsso, "Magnetic force microscopy investigation of domain structure in Fe- x at.% Ga single crystals ($12 < x < 25$)," *J. Appl. Phys.* **98**, 023904 (2005).
- O. Ikeda, R. Kainuma, I. Ohnuma, K. Fukamichi, and K. Ishida, "Phase equilibria and stability of ordered b.c.c. phases in the Fe-rich portion of the Fe-Ga system," *J. Alloys Compd.* **347**, 198–205 (2002).
- Phase Diagram of Binary Iron Alloys*, Monographs Series on Alloy Phase Diagrams Vol. 9, edited by H. Okamoto (ASM International, Materials Park, USA, 1993), ISBN 978-0-87170-403-0.
- N. Kawamiya, K. Adachi, and Y. Nakamura, "Magnetic properties and Mössbauer investigations of Fe-Ga alloys," *J. Phys. Soc. Jpn.* **33**(5), 1318–1327 (1972).
- C. J. Quinn, P. J. Grundy, and N. J. Mellors, "The structural and magnetic properties of rapidly solidified Fe_{100-x}Ga_x alloys, for $12.8 \leq x \leq 27.5$," *J. Magn. Magn. Mater.* **361**, 74–80 (2014).
- I. S. Golovin, V. V. Palacheva, A. Emdadi, D. Mari, A. Heintz, A. M. Balagurov, and I. A. Bobrikov, "Anelasticity of phase transitions and magnetostriction in Fe-(27%–28%)Ga alloys," *Mater. Res.* **21**(2), e20170906 (2018).
- A. Embadi, V. V. Palacheva, A. M. Balagurov, I. A. Bobrikov, V. V. Cheverikin, J. Cifre, and I. S. Golovin, "Tb-dependent phase transitions in Fe-Ga functional alloys," *Intermetallics* **93**, 55–62 (2018).
- Y. Han, H. Wang, T. Zhang, Y. He, and C. Jiang, "Exploring structural origin of the enhanced magnetostriction in Tb-doped Fe₈₃Ga₁₇ ribbons: Tuning Tb solubility," *Scr. Mater.* **150**, 101–105 (2018).
- T. Zhou, Y. Zhang, D. Luan, and Q. Cai, "Effect of cerium on structure, magnetism and magnetostriction of Fe₈₁Ga₁₉ alloy," *J. Rare Earths* **36**, 721–724 (2018).
- A. Javed, T. Szumiata, N. A. Morley, and M. R. J. Gibbs, "An investigation of the effect of structural order on magnetostriction and magnetic behaviour of Fe-Ga alloy thin films," *Acta Mater.* **58**, 4003–4011 (2010).
- G. A. Ramirez, F. Malamud, J. E. Gómez, L. M. Rodríguez, D. Fregenal, A. Butera, and J. Milano, "Controlling the crystalline and magnetic texture in sputtered Fe_{0.89}Ga_{0.11} thin films: Influence of substrate and thermal treatment," *J. Magn. Magn. Mater.* **483**, 143–151 (2019).
- A. McClure, S. Albert, T. Jaeger, H. Li, P. Rugheimer, J. A. Schaefer, and Y. U. Idzerda, "Properties of single crystal Fe_{1-x}Ga_x thin films," *J. Appl. Phys.* **105**, 07A938 (2009).
- X. Liu, M. Li, J. Gou, Q. Li, Y. Lu, T. Ma, and X. Ren, "Evidence for lattice softening of the Fe-Ga magnetostrictive alloy: Stress-induced local martensites," *Mater. Des.* **140**, 1–6 (2018).
- M. Ciria, M. G. Proietti, E. C. Corredor, D. Coffey, A. Bégue, C. de la Fuente, J. I. Arnaidas, and A. Ibarra, "Crystal structure and local ordering in epitaxial Fe_{100-x}Ga_x/MgO(001) films," *J. Alloys Compd.* **767**, 905–914 (2018).
- A. E. Clark, K. B. Hathaway, M. Wun-Fogle, J. B. Restorff, T. A. Lograsso, V. M. Keppens, G. Petculescu, and R. A. Taylor, "Extraordinary magnetoelasticity and lattice softening in bcc Fe-Ga alloys," *J. Appl. Phys.* **93**, 8621 (2003).
- N. Srisukhumbowornchai and S. Guruswamy, "Influence of ordering on the magnetostriction of Fe-27.5 at.% Ga alloys," *J. Appl. Phys.* **92**, 5371 (2002).
- A. K. Mohamed, V. V. Palacheva, V. V. Cheverikin, E. N. Zanaeva, W. C. Cheng, V. Kulitckii, S. Divinski, G. Wilde, and I. S. Golovin, "The Fe-Ga phase diagram: Revisited," *J. Alloys Compd.* **846**, 156486 (2020).
- T. Jin, H. Wang, I. S. Golovin, and C. Jiang, "Microstructure investigation on magnetostrictive Fe_{100-x}Ga_x and (Fe_{100-x}Ga_x)_{99.8}Tb_{0.2} alloys for $19 < x < 29$," *Intermetallics* **115**, 106628 (2019).
- Z. Nie, Z. Wang, Y. Liang, D. Cong, G. Li, C. Zhu, C. Tan, X. Yu, Y. Ren, and Y. Wang, "Structural investigations of Fe-Ga alloys by high-energy x-ray diffraction," *J. Alloys Compd.* **763**, 223–227 (2018).
- W. Lefebvre-Ulrikson, F. Vurpillot, and X. Sauvage, *Atom Probe Tomography: Put Theory into Practice* (Elsevier, 2016), ISBN 978-0-12-804647-0.
- B. Gault, M. P. Moody, J. M. Cairney, and S. P. Ringer, *Atom Probe Tomography* (Springer, 2012).
- IVAS³.8 User Guide (2016).
- I. S. Golovin, A. M. Balagurov, I. A. Bobrikov, S. V. Sumnikov, and A. K. Mohamed, "Cooling rate as a tool of tailoring structure of Fe-(9%–33%)Ga alloys," *Intermetallics* **114**, 106610 (2019).
- I. S. Golovin, A. K. Mohamed, I. A. Bobrikov, and A. M. Balagurov, "Time-temperature-transformation from metastable to equilibrium structure in Fe-Ga," *Mater. Lett.* **263**, 127257 (2020).
- K. Momma and F. Izumi, "VESTA 3 for three-dimensional visualization of crystal, volumetric and morphology data," *J. Appl. Crystallogr.* **44**, 1272–1276 (2011).

- ³³F. Richomme, A. Fnidiki, J. Teillet, and M. Toulemonde, "Tb/Fe amorphous multilayers: Transformations under ions irradiation," *Nucl. Instrum. Methods Phys. Res., Sect. B* **107**, 374–380 (1996).
- ³⁴J. P. Eymery, A. Fnidiki, and J. P. Riviere, "CEMS as applied to implantation studies in Fe-Al 40 at.%, " *Nucl. Instrum. Methods Phys. Res.* **209-210**, 919–924 (1983).
- ³⁵J. Juraszek, O. Zivotsky, H. Chiron, V. Vaudolon, and J. Teillet, "A setup combining magneto-optical Kerr effect and conversion electron Mössbauer spectrometry for analysis of the near-surface magnetic properties of thin films," *Rev. Sci. Instrum.* **80**, 043905 (2009).
- ³⁶A. Fnidiki, F. Richomme, J. Teillet, F. Pierre, P. Boher, and Ph. Houdy, "Tb/Fe multilayers: A study by conversion electron Mössbauer spectrometry and polar Kerr effect," *J. Magn. Magn. Mater.* **121**, 520–523 (1993).
- ³⁷K. M. Hamasha, I. A. Al-Omari, and S. H. Mahmood, "Mössbauer and structural studies of the $\text{Fe}_2\text{Cr}_{1-x}\text{V}_x$ alloy system," *Physica B* **321**, 154–158 (2002).
- ³⁸A. Fnidiki, C. Lemoine, and J. Teillet, "Properties of mechanically alloyed $\text{Fe}_{100-x}\text{Cr}_x$ powder mixtures: Mössbauer study," *Physica B* **357**, 319–325 (2005).
- ³⁹G. Charitou, C. Tsertos, Y. Parpottas, M. Kleanthous, C. W. Lederer, and M. Phylactides, " ^{57}Fe enrichment in mice for β -thalassaemia studies via Mössbauer spectroscopy of blood samples," *Eur. Biophys. J.* **48**, 635–643 (2019).
- ⁴⁰E. Bill, " ^{57}Fe -Mössbauer spectroscopy and basic interpretation of Mössbauer parameters," in *Practical Approaches to Biological Inorganic Chemistry, 2nd edition* (Elsevier, 2020), pp. 201–228.
- ⁴¹H. E. Stauss, "Measurement of the linear magnetostriction of hard-worked nickel," *J. Appl. Phys.* **30**, 1648–1650 (1959).
- ⁴²L. R. Newkirk and C. C. Tsuei, "Mössbauer study of BiF_3 -type ordering in metastable FeGa alloys," *J. Appl. Phys.* **42**, 5250 (1971).
- ⁴³H. Cao, F. Bai, J. Li, D. D. Viehland, T. A. Lograsso, and P. M. Gehring, "Structural studies of decomposition in Fe-x at.%Ga alloys," *J. Alloys Compd.* **465**, 244–249 (2008).
- ⁴⁴J. Boisse, H. Zapolsky, and A. G. Khachatryan, "Atomic-scale modeling of nanostructure formation in Fe-Ga alloys with giant magnetostriction: Cascade ordering and decomposition," *Acta Mater.* **59**(7), 2656–2668 (2011).
- ⁴⁵J. M. Borrego, J. S. Blázquez, C. F. Conde, A. Conde, and S. Roth, "Structural ordering and magnetic properties of arc-melted FeGa alloys," *Intermetallics* **15**(2), 193–200 (2007).
- ⁴⁶F. Stein, A. Schneider, and G. Frommeyer, "Flow stress anomaly and order-disorder transitions in Fe_3Al -based Fe-Al-Ti-X alloys with $X = \text{V}, \text{Cr}, \text{Nb}, \text{or Mo}$," *Intermetallics* **11**, 71–82 (2003).
- ⁴⁷H. W. Williams and B. L. Chamberland, "Determination of Curie, Néel, or crystallographic transition temperature via differential scanning calorimetry," *Anal. Chem.* **41**(14), 2084–2086 (1969).
- ⁴⁸R. Barua, P. Taheri, Y. Chen, A. Koblichka-Veneva, M. R. Koblichka, L. Jiang, and V. G. Harris, "Giant enhancement of magnetostrictive response in directionally-solidified $\text{Fe}_{83}\text{Ga}_{17}\text{Er}_x$ compounds," *Materials* **11**, 1039 (2018).
- ⁴⁹P. Gabriela, R. Wu, and R. McQueeney, "Magnetoelasticity of bcc Fe-Ga alloys," *Handb. Mag. Mater.* **20**, 123–226 (2012).
- ⁵⁰F. Bai, H. Zhang, J. Li, and D. Viehland, "Magnetic force microscopy investigation of the static magnetic domain structure and domain rotation in Fe-x at. % Ga alloys," *Appl. Phys. Lett.* **95**, 152511 (2009).
- ⁵¹J. Zhang, T. Ma, and M. Yan, "Magnetic force microscopy study of heat-treated $\text{Fe}_{81}\text{Ga}_{19}$ with different cooling rates," *Physica B* **405**, 3129–3134 (2010).
- ⁵²C. Mudivarthi, S.-M. Na, R. Schaefer, M. Laver, M. Wuttig, and A. B. Flatau, "Magnetic domain observations in Fe-Ga alloys," *J. Magn. Magn. Mater.* **322**, 2023–2026 (2010).
- ⁵³E. Ferrara, E. Olivetti, F. Fiorillo, E. Forton, L. Martino, and L. Rocchino, "Microstructure and magnetic properties of pure iron for cyclotron electromagnets," *J. Alloys Compd.* **615**, S291–S295 (2014).
- ⁵⁴H. D. Chopra and M. Wutting, "Non-joulian magnetostriction," *Nature* **521**, 340 (2015).